Lagrangian Tools for the Analysis of Mixing in Single-Phase and Multiphase Flow Systems

Antonio Guida, Alvin W. Nienow, and Mostafa Barigou
School of Chemical Engineering, University of Birmingham, Edgbaston, Birmingham, B15 2TT, U.K.

DOI 10.1002/aic.12557
Published online March 18, 2011 in Wiley Online Library (wileyonlinelibrary.com).

Mixing is intrinsically a Lagrangian process and, while Eulerian data are very important, Lagrangian information is necessary for its complete description. Lagrangian data can, in principle, be generated by using numerical simulations or experimental techniques based on Lagrangian tracking to provide the trajectories of fluid elements or particles. We present a set of theoretical and computational tools specifically developed for the analysis and validation of single-phase and multiphase Lagrangian flow data obtained from tracer trajectories in mechanically agitated vessels. The implementation and power of these tools are demonstrated by analyzing a wide range of measurements acquired using the technique of positron emission particle tracking during mixing of Newtonian and non-Newtonian fluids as well as mixing of concentrated solid–liquid suspensions. Finally, the accuracy of the raw Lagrangian data treatment developed here is illustrated by comparing with an Eulerian technique and showing very precise mass continuity for an agitated solid–liquid system. © 2011 American Institute of Chemical Engineers *AIChE J,* 58: 31–45, 2012
Keywords: Lagrangian tracking, mixing, PEPT, solid distribution, solid–liquid flow, stirred vessel

Introduction

Mechanically agitated vessels are widely used across a diverse range of industries including the chemical, food, pharmaceutical, mineral, nuclear, and petroleum industries. In the last few decades, the need to properly design or optimize mixing equipment and processes has motivated numerous studies aiming to develop a deep understanding of the complex local hydrodynamics of single-phase and multiphase systems within such stirred vessels. Recently, laser Doppler velocimetry (LDV) or particle image velocimetry (PIV) has been used to examine the complex nature of the flow fields in transparent single-phase systems.[1–3] Such approaches have also been reasonably successful at obtaining Eulerian data for the liquid phase in very dilute two-phase systems.[4,5] These optical techniques, however, only provide Eulerian data while mixing is intrinsically a Lagrangian process.

Lagrangian data can, in principle, be obtained by using either numerical simulation or ''non-intrusive'' experimental techniques based on Lagrangian tracking to provide the trajectories of fluid elements or of solid particles in a flow system. For example, by numerically simulating the paths taken by 100,000 particles released at three different points, LaRoche[6] studied the effect of the position of the feed point on the mixing efficiency inside a stirred vessel. The different behavior in the suspension of three sizes of heavy particles within a mixing vessel was recently simulated using Lagrangian particle tracking and direct numerical simulation of turbulence.[7] Experimental techniques which are effective in providing Lagrangian data in flow systems, however, are very limited.[8,9] A number of authors have shown that the analysis of Lagrangian data obtained from a single particle trajectory allows important mixing information to be obtained which is not measurable by Eulerian observations.[8–11]

Correspondence concerning this article should be addressed to M. Barigou at m.barigou@bham.ac.uk.

Positron emission particle tracking (PEPT) represents a recent and improved addition to the experimental techniques available for Lagrangian studies, particularly useful for the very complex three-dimensional (3-D) flow fields found in agitated vessels. It allows non-invasive probing of opaque fluids within an opaque apparatus using a single sub-millimetre positron-emitting tracer particle. It accurately tracks the particle in 3-D space and time with better spatial and temporal resolution than other Lagrangian methods (though not as good as those which are laser-based) throughout the whole of the vessel to reveal its Lagrangian trajectory.[12,13] PEPT is particularly valuable for the study of opaque systems whether single-phase or multiphase, or for multicomponent solid–liquid flows where one size can be selectively labeled and its behavior observed.[14–17]

To maximize the usefulness of the experimental Lagrangian data obtained by PEPT, a set of theoretical and computational tools have been developed and used for the analysis and validation of different sets of data. As they are suitable for use in handling Lagrangian tracer trajectories in general whether obtained numerically via computer simulation or experimentally using PEPT or any other advanced particle tracking technique, that development work is described here. In order for the approach to be illustrated, the sets of Lagrangian data used come from experimental data using PEPT.

Data Collection

Lagrangian tracking is based on the study of data obtained following the long-term trajectory of a particle tracer either numerically or experimentally. Therefore, the starting point of the data analysis is the knowledge of the position of the particle tracer in space at multiple instants which can be expressed by the four time-space arrays $[t_k]$, $[x_k]$, $[y_k]$, and $[z_k]$ where k is a location counter. It must be stressed that obtaining accurate data of this kind is not a trivial matter. Although the equipment used to provide the Lagrangian data analyzed here has been described previously,[15] to aid the reader the critical aspects of the experimental technique are briefly summarized here as well as the mixing processes examined which include low-viscosity highly turbulent single-phase flows, shear-thinning laminar/transitional paste mixing, and the mixing of highly concentrated, turbulent binary solid–liquid suspensions.

Experimental particle tracking

In the particular case of PEPT, the technique primarily involves the use of a labeled particle tracer, a positron camera, and a location algorithm for computing the tracer location. The tracer particle is labeled with a positron-emitting nuclide and the radio isotopes usually used are ^{18}F, ^{61}Cu, and ^{66}Ga. Isotope ^{18}F has a half-life of 109 min and is produced from either purified water or solid materials under direct bombardment with high energy (33 MeV) ^{3}He beams via the reactions

$$^{16}\mathrm{O}\left(^{3}\mathrm{He},p\right)^{18}\mathrm{F} \text{ or } ^{16}\mathrm{O}\left(^{3}\mathrm{He},n\right)^{18}\mathrm{Ne} \rightarrow {}^{18}\mathrm{F} \qquad (1)$$

The ^{3}He nuclei are accelerated *in situ* by using a cyclotron. Similarly, the reaction

$$^{60}\mathrm{Ni}(d,n)^{61}\mathrm{Cu} \qquad (2)$$

is induced to produce ^{61}Cu, having a half-life of 3.3 h, by irradiating natural nickel with deuterons. The gallium radionuclide ^{66}Ga has a half-life of 9.3 h and is produced from zinc foils via the reaction

$$^{66}\mathrm{Zn}(p,n)^{66}\mathrm{Ga} \qquad (3)$$

The separation of trace amounts of copper (gallium) radioisotopes from nickel (zinc) foils is conducted by cation chromatography. The techniques currently used for particle labeling are surface modification,[18] direct irradiation and ion exchange.[19]

A positron emitted by the particle tracer rapidly annihilates with an electron emitting a pair of almost collinear 511 keV γ-quanta in opposite directions. The detection in coincidence of these two γ-rays by the positron camera is the first step in locating the tracer. The positron camera consists of two γ-camera heads working in coincidence and mounted on a motorized gantry which allows their rotation about a horizontal axis. Each head contains a single sodium iodide crystal optically coupled to an array of photomultiplier tubes.[20] When a positron-electron annihilation occurs, the γ-rays emitted produce two coincident scintillations in the crystals, the related photomultipliers generate positional signals and two two-dimensional (2-D) centroids are calculated by the detection software (Figure 1). The joining line is the photon-trajectory related to the annihilation event. With a small number of annihilation events (theoretically only two), the position of a single positron-emitting particle can be located at the intersection of the photon-trajectories.

The location algorithm calculates the time-space location of the radioactive tracer minimizing the sum of perpendicular distances from a generic point to the various photon-trajectories.[21] Moreover, it discards iteratively the corrupt events caused by Compton scattering, the radioactive background or if the two detected γ-rays were not in fact a pair of 511 keV photons originating from the same positron-electron annihilation event.

Mixing systems examined

A broad set of single particle tracking experiments were conducted on single-phase and solid–liquid systems in fully baffled flat-base cylindrical vessels[17,22,23] having a diameter T varying in the range 150–290 mm (Figure 1). Newtonian and non-Newtonian single-phase fluids were used to study mixing under turbulent and laminar/transitional flow conditions including cavern formation, using neutrally buoyant particle tracers. Nearly monomodal and nearly spherical glass beads with a diameter d in the range 1–3.3 mm were used to make monodisperse, binary and polydisperse slurries where the suspending medium was usually an aqueous NaCl solution. The mean solid mass concentration, X, was varied in the range 0–40 wt %. The level of the single-phase fluid or solid–liquid suspension in the tank was kept at $H = T$ for all the experiments. Solid–liquid mixing experiments were conducted at the minimum rotational speed for particle suspension, N_{js}, determined experimentally according to the well-known Zwietering criterion,[24] i.e., no particle should

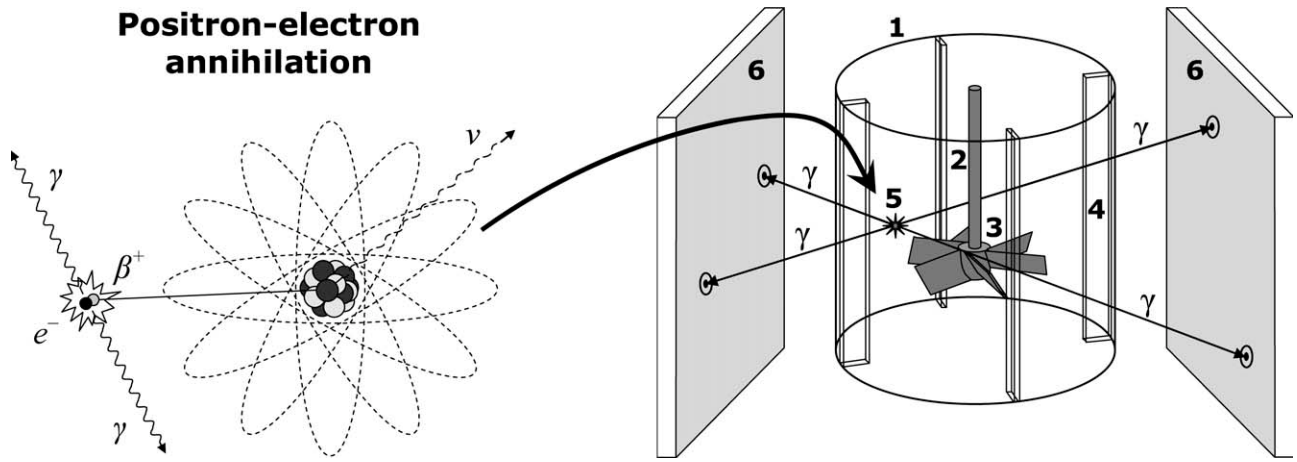

Figure 1. Schematic illustration of positron-electron annihilation and experimental PEPT set-up: 1, tank; 2, shaft; 3, impeller; 4, baffle; 5, radioactive tracer; 6, γ-ray detectors.

remain stationary on the base of the vessel for longer than 1–2 s. The agitator used was a 6-blade 45° pitched blade turbine (PBT) pumping downward (PBTD) or upward (PBTU). Its diameter, D, was varied in the range 0.33–0.55 T and its off-bottom clearance was set at 0.25 T or 0.33 T.

In a multiphase system, the flow behavior of the different phases is expected to be different; therefore, each phase component should be tracked separately. In a monodisperse suspension, where the number of components is equal to the number of phases (solid and liquid), two sets of trajectory data are required to properly describe the suspension. Similarly, for a binary suspension with two particle size fractions, three separate sets of trajectory data describing the three components are required, i.e., one liquid phase component and two solid phase components. More generally, a polydisperse suspension consisting of n_s different size fractions of particles requires $n_s + 1$ separate trackings.

This method which, by its very nature, is based on a discrete approach could be generalized to study solid–liquid systems which are characterized by a continuous particle-size distribution (PSD). If the average PSD within the agitated solid–liquid system is known and does not significantly vary during mixing (e.g., due to breakage, dissolution, or agglomeration), the system can be studied by single particle tracking. Once the average PSD has been discretized into multiple bins, the average flow behavior of each solid component representing a given bin can be investigated by tracking a particle tracer with a size falling into that bin. The inherent error related to this approach becomes small when the PSD is discretized using a large number of bins.

Selective labeling in multicomponent systems

As explained above, in the case of a multicomponent system, the full 3-D trajectory of each component must be resolved separately. Currently, PEPT can most accurately track one particle at a time. For this reason, multicomponent investigations consist of multiple successive and distinct experiments: two for a monodisperse suspension, three for a binary suspension and $n_s + 1$ for a polydisperse suspension. Resin tracers radioactively labeled with ^{18}F by ion exchange have usually been used to track the liquid phase. They can be as small as 250 μm and have a density slightly higher than water. The resin particle tracer is made neutrally buoyant by using an aqueous NaCl solution whose salt concentration is adjusted to match the density of the tracer. Each solid component is tracked using a representative glass bead of the examined particle size fraction, which is directly irradiated by means of a cyclotron and, therefore, enriched in ^{18}F via the nuclear reactions in Eq. 1.

Lagrangian-Eulerian Analysis

Two kinds of data analysis are presented in this work: first, a Lagrangian-Eulerian analysis used to extract Eulerian information from the purely Lagrangian information contained in the tracer trajectory; and second, a Lagrangian-statistical analysis exploiting concepts such as residence time, circulation time and trajectory length distribution (TLD), obtainable only when Lagrangian data are available. The structure of the computational code developed for extracting Eulerian information consists of a set of subroutines containing different algorithms created to progressively analyze the initial Lagrangian data and store important intermediate outputs. Because of the varied nature of the mixing systems examined, the code had to be flexible enabling key-parameters to be set and specific subroutines to be activated or deactivated as required.

Direct trajectory visualization

The conversion of the input file in four numerical arrays $[t_k]$, $[x_k]$, $[y_k]$, and $[z_k]$ is the first step in the data analysis. Plotting values of the spatial coordinates x, y, and z, in 3-D space generates images similar to those in Figure 2 which show the extent of the regions visited by the tracer. In Figure 2a, where the neutrally buoyant particle is tracking a single-phase in turbulent flow ($\mathrm{Re_{imp}} \sim 40{,}000$), the entire volume is very rapidly covered. The complexity of the trajectory also gives a visual impression of the quality of fluid mixing inside the vessel. In the mixing of viscoplastic fluids which exhibit an apparent yield stress, the impeller creates a cavern within

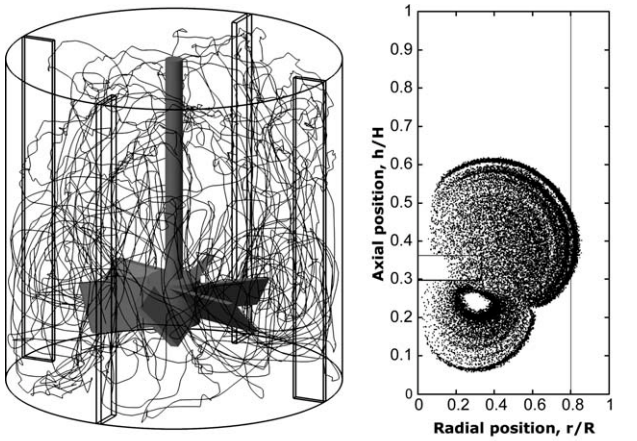

Figure 2. Illustration of Lagrangian tracking: (a) fluid trajectory in a turbulent system ($Re_{imp} \sim 40{,}000$); (b) cavern visualization in low transitional flow in a viscoplastic fluid with an apparent yield stress ($Re_{imp} \sim 70$)—figure shows the locus of tracer locations within cavern.

which fluid is in flow, but in the bulk where the shear stresses are below the yield stress, the fluid is stagnant.[25] In this case, the particle tracer visits only a portion of the vessel volume delineating the boundaries of the cavern formed (Figure 2b), which allows an accurate estimation of the cavern volume and gives a detailed description of the flow field within, information which has hitherto been impossible to obtain in opaque fluids.

PEPT location filter

When using PEPT experimental data, a basic step in their analysis is the elimination of the occasionally corrupt locations not discarded by the initial PEPT reconstruction algorithm, which may be caused by spurious radioactivity from the surroundings, scattering phenomena or a too short time interval between two consecutive positron emissions. To efficiently remove such corrupt locations, a filter function needs to operate locally taking into account the probability of tracer detection and local flow velocity.

The 3-D flow field in a mixing vessel is very complex and is often characterized by high local velocity gradients. Assuming a constant frequency of acquisition of the 3-D locations of the positron-emitting particle tracer, an acceleration of the tracer creates a dilation of the curvilinear distance separating two consecutively detected locations along the trajectory; therefore, in the presence of a high velocity, the density of tracer detections along the trajectory would be reduced. However, the frequency of data acquisition is not constant as the probability of its detection varies with its location. Figure 3a is a 2-D illustration of how the location of the tracer can affect the probability of detection. Knowledge of the expected density of tracer detections along the trajectory can be used to realize a filter function which efficiently identifies and discards occasionally corrupt locations.

The probability of tracer detection can be assumed — to a first approximation — to be proportional to the geometric efficiency of detection which can be calculated through geometric considerations. Such an approximation is reasonable because other factors (or their variation with tracer position) affecting the detection ability and accuracy of PEPT are of a secondary order compared with the geometric efficiency (or its variation with tracer position), including the possibility that two decay events occur in the same time window, the range of positrons in matter before annihilation with an electron, the fact that the γ-rays are not exactly 180° apart (±0.5°), photon absorption/scattering phenomena, and the angle at which the γ-rays pass through the crystal inside the detector.

The infinitesimal probability that one γ-ray will travel inside the solid angle, $d\Omega$, subtended at the source by an infinitesimal area of a detector can be expressed by normalizing this angle by the total solid angle (4π). Considering that two γ-rays are emitted, the infinitesimal probability, dE_G, that one of the two photons will travel inside $d\Omega$ can then be written as:

$$dE_G = 2\frac{d\Omega}{4\pi} \tag{4}$$

Expressing the solid angle $d\Omega$ in spherical coordinates with the origin being located at the instantaneous position of the particle tracer (x, y, z) as shown in Figure 3b, Eq. 4 becomes:

$$dE_G = \frac{\sin\phi d\theta d\phi}{2\pi} \tag{5}$$

The geometric efficiency, E_G, can thus be imagined as the sum of such infinitesimal contributions whose values of θ and ϕ allow the direction of the γ-rays to intersect both detectors; therefore, double integration in θ and ϕ allows the geometric efficiency to be analytically determined. By applying geometric considerations, the zenithal integration limits can be obtained from Figure 3b as functions of the azimuth θ; thus:

$$\phi_{min} = \arctan\left(\max\left\{\frac{S_D - 2y}{H_D - 2z}; \frac{S_D + 2y}{H_D + 2z}\right\}\csc\,\theta\right) \tag{6}$$

and

$$\phi_{max} = \pi - \arctan\left(\max\left\{\frac{S_D - 2y}{H_D + 2z}; \frac{S_D + 2y}{H_D - 2z}\right\}\csc\,\theta\right) \tag{7}$$

The maximum function which is present in both Eqs. 6 and 7 derives from the condition that both the γ-rays must intersect a detector. In a similar manner, the azimuthal integration limits can be determined using Figure 3b, thus:

$$\theta_{min} = \arctan\left(\max\left\{\frac{S_D - 2y}{L_D - 2x}; \frac{S_D + 2y}{L_D + 2x}\right\}\right) \tag{8}$$

and

$$\theta_{max} = \pi - \arctan\left(\max\left\{\frac{S_D - 2y}{L_D + 2x}; \frac{S_D + 2y}{L_D - 2x}\right\}\right) \tag{9}$$

A first complete expression of the geometric efficiency, E_G, is established by evaluating the inner integral ϕ and then using basic trigonometric identities, namely:

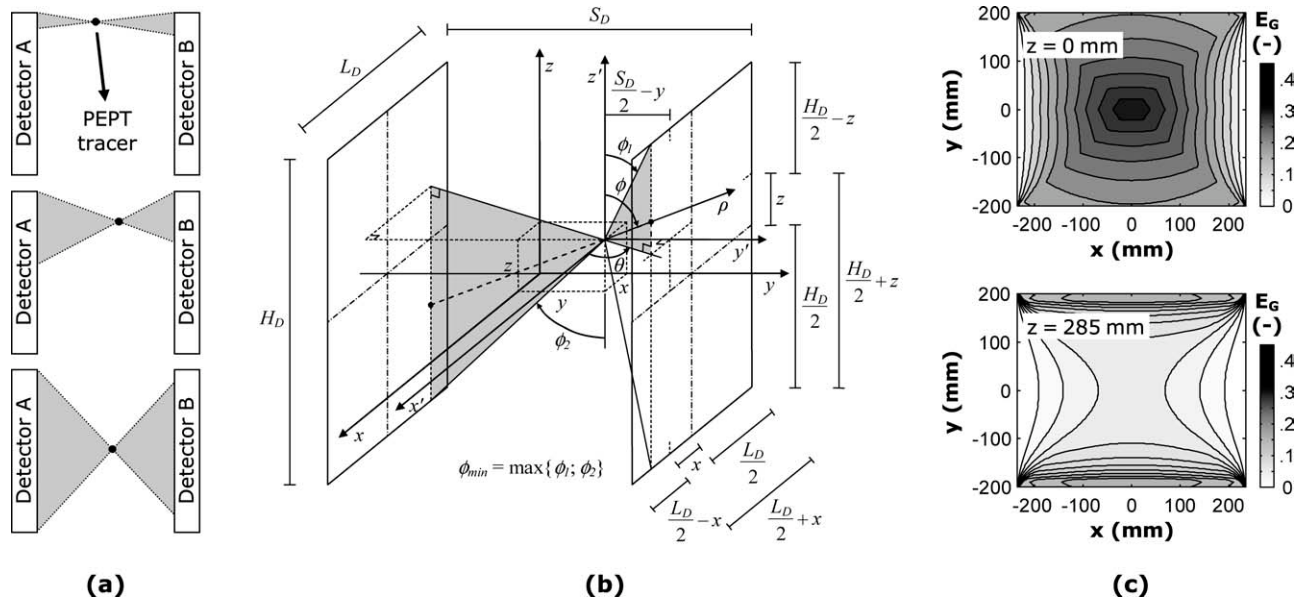

Figure 3. PEPT geometric efficiency of detection: (a) two-dimensional representation of its dependency on the angle subtended at the source by both detectors; (b) illustration of the derivation of the E_G function; (c) horizontal *xy* maps of geometric efficiency at two different vertical coordinates for S_D = 400 mm.

$$E_G = \frac{1}{2\pi}\sum_{q=1}^{2}\int_{\theta_{min}}^{\theta_{max}}\left(\max\left\{\frac{S_D - 2y}{H_D + (-1)^q 2z};\ \frac{S_D + 2y}{H_D - (-1)^q 2z}\right\}^2 \csc^2\theta + 1\right)^{-\frac{1}{2}} d\theta \qquad (10)$$

The last outer integral can also be evaluated analytically leading, however, to a very long expression which, on the other hand, does not exhibit any trigonometric or integral functions. The obtained geometric efficiency $E_G = E_G(x, y, z, L_D, H_D, S_D)$ becomes a 3-D function (only position dependent), for a given width, L_D, and height, H_D, of the rectangular active area of the γ-ray detectors, with a separation, S_D, between them. Note that as L_D and H_D are fixed by the size of the detectors' active area (470 × 590 mm^2 for the Birmingham Positron Camera), S_D can be varied up to a maximum of 800 mm to suit the size of the flow system under investigation. Two-dimensional maps of the geometric efficiency are depicted in Figure 3c at selected heights within the detection space, for a fixed detector separation S_D = 400 mm. E_G is maximum at the origin of coordinates, i.e., at the centre of the detection space, and is zero at the edges. Consequently, the probability and, hence, the number of successfully detected positions of a particle tracer tend to be highest in the centre between the detectors. In addition, the probability of detection is increased with increasing detector size, L_D and H_D, and for a given size, by reducing S_D.

As pointed out above, in high velocity zones, the density of tracer detections along the trajectory decreases while in regions where the probability of tracer detection is high, such a density increases. In a stirred vessel, the central region should be affected most by high local velocities, but at the same time the probability of tracer detection there is the highest. On the other hand, near the boundaries of the vessel, the velocities are smaller but the probability of detection is lower. Consequently, these two effects tend to approximately cancel each other for an accurately centered tank with dimensions not too close to those of the detectors, and for a separation such that $H_D > S_D > L_D$ or $L_D > S_D > H_D$, so that for $L_D \sim H_D$ the detection space is approximately cubical. Nonetheless, for better accuracy, the filter function operates locally, as pointed out above, and the threshold used to discard occasionally corrupted locations is calculated as a function of the local values of geometric efficiency and the expected magnitude of the local flow velocity.

Location of the vessel axis

An accurate and precise location of the vertical vessel axis (x_0, y_0) and base (z_0) is crucial to correctly define a new system of cylindrical coordinates (ϑ, r, h), which is required for the Eulerian description of a cylindrical mixing vessel. Manual determination of its position without specialized equipment can lead to significant errors. Measuring the coordinates of a static tracer placed in specific key-positions by PEPT, however, enables the three coordinates x_0, y_0, and z_0 to be accurately located.

This calibration can be avoided when the particle tracer visits every region of the vessel and the vessel boundaries are clearly traced, e.g., in a turbulent system with a sufficiently long runtime. However, vessel centering should not be based on the assumption that the average position of the particle tracer which approximately corresponds to the mean value of the arrays $[x_k]$, $[y_k]$, and $[z_k]$, defines the centre of the tank. There is no certainty that the tracer is detected an equal number of times in every region; it could be detected more frequently in some areas than others for various reasons including temporary tracer immobility, for example in a stagnant region or behind a baffle, and non-uniformity of the

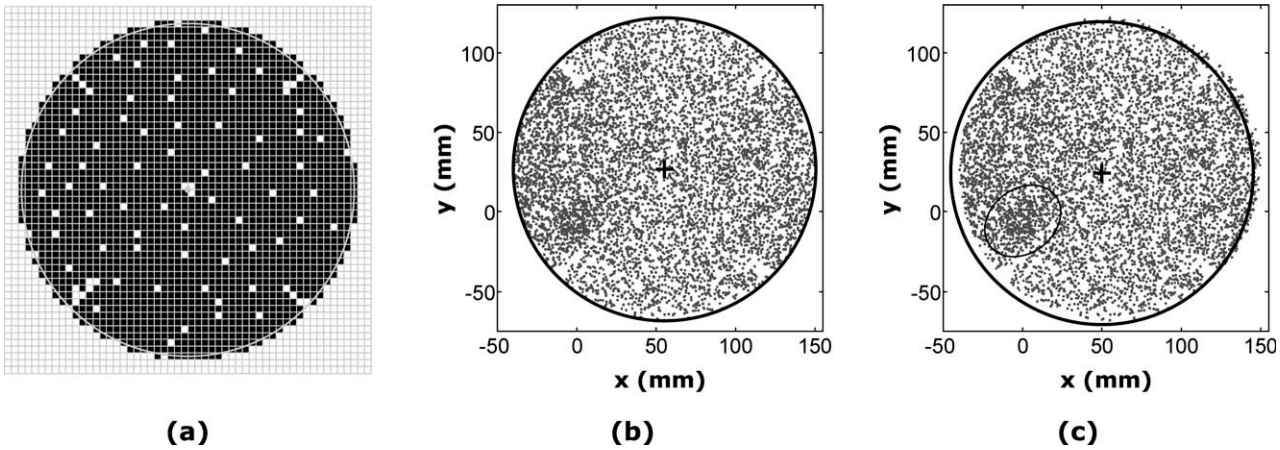

Figure 4. Location of the vessel axis: (a) pixelized projection of the tracer locations onto a horizontal plane (note the pixel size has been exaggerated for clarity); (b) axis location by data analysis routine; (c) axis location using the average values of the coordinates *x* and *y* (the ellipse delineates a region of high location density causing off-centring of the vessel).

geometric efficiency for vessels not perfectly placed in the centre of the active area of detection. This problem is circumvented when each location is projected onto a horizontal plane (xy) and such a plane is "pixelized"; numerous locations within the same pixel having similar horizontal coordinates x and y are represented by a single pixel regardless of their number and vertical coordinate z (Figure 4a). Such a pixelized horizontal projection contains "black" pixels which are positions occupied by the tracer, and "white" pixels which are positions never visited by the tracer. Assuming a centre and starting from a circumference with radius r_c slightly smaller than $T/2$, the fraction of black pixels q_b intersected by such a circumference is computed. Thus, the ratio q_b is recalculated increasing gradually the radius of the circumference to a value slightly higher than $T/2$. The true centre of the pixel map, corresponding to the vessel axis position, is characterized by the sharpest drop of q_b from ~ 1 to ~ 0 when increasing r_c. Based on the same principles, the position of the vessel base z_0 can be obtained using a simpler one-dimensional projection on a vertical straight line.

The accuracy in the above procedure is increased by reducing the pixel size which is usually a fraction of a millimeter; however, the pixel dimensions shown in Figure 4a have been exaggerated to illustrate the process. In Figures 4b, and 4c, the performance of the subroutine (Figure 4b) is compared with the result obtained using the average values of the arrays $[x_k]$ and $[y_k]$ to identify the vessel axis location (x_0, y_0) (Figure 4c). The tracer locations outside the vessel boundary indicate that this last procedure may lead to a wrongly positioned vessel axis. For the particular set of data shown in Figure 4, the large error obtained using the average position of the particle tracer is engendered by a non-uniform density of locations which is higher within the region delineated by the ellipse in Figure 4c and, consequently, causes the vessel axis location (x_0, y_0) to be shifted toward this region.

Dummy locations

The code uses a 3-D user-defined grid consisting of a large number of equal volume cells, n_c, to obtain an Eulerian description of the flow field inside the vessel, based on values of velocity and other quantities determined in each grid cell. Such a cylindrical grid is made up of three kinds of hyperplanes: radial-axial planes ($\vartheta = \text{const}$), cylindrical hyperplanes ($r = \text{const}$), and horizontal planes ($h = \text{const}$). The degree of fineness of the grid is directly related to the error inherent in the discrete approach. The lower limit of the size of a grid cell which minimizes such an error component is usually dictated by experimental factors such as data acquisition rate, tracking runtime, location error of the technique, and average Lagrangian velocity of the particle tracer.

For accurate data analysis, it is also important to deal with the occasional short interruptions (>50 ms) in the trajectory caused by the occurrence, very occasionally, of incidents that lead to a low frequency of data acquisition. A typical example in the case of PEPT is when a particle tracer which, after hours of experimentation, has lost most of its beta activity, travels at very high speed across a region of low geometric efficiency (Figure 3c). The effect of such short trajectory interruptions is usually negligible but should not be ignored when the tracer is moving at a particularly high velocity. Where there are interruptions in the tracking of the tracer, it is not usually possible to be certain about where the tracer has been during this time, but it is possible as a first approximation to define a linear segment of trajectory between the last and the next detected location, assuming that the tracer moves at a constant velocity between the two points. As shown in Figure 5, the equation of a hyperplane and the two equations of such a 3-D linear segment define a system of three equations which, in the case of a radial-axial vertical plane (say at $\vartheta = \vartheta^*$), can be expressed by:

$$\begin{cases} (y - y_0) = (x - x_0)\tan\vartheta^* \\ y = a_1 x + b_1 \\ z = a_2 x + b_2 \end{cases} \tag{11}$$

where Cartesian coordinates are used and the coefficients a_1, a_2, b_1, and b_2 are calculated using the coordinates of the last and the next detected location. In the case of a cylindrical

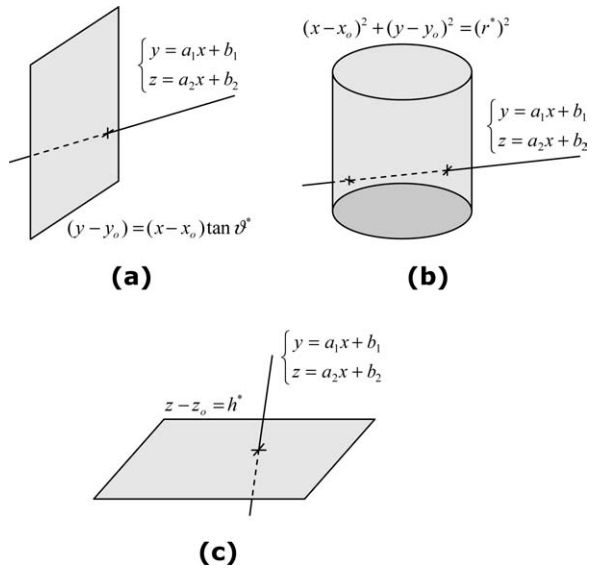

Figure 5. Intersection of a 3-D straight line with hyperplanes at (a) $\vartheta = \vartheta^*$; (b) $r = r^*$; (c) $h = h^*$.

hyperplane (say at $r = r^*$) or a horizontal plane (say at $h = h^*$), the above system of equations becomes, respectively:

$$\begin{cases} (x - x_0)^2 + (y - y_0)^2 = (r^*)^2 \\ y = a_1x + b_1 \\ z = a_2x + b_2 \end{cases} \tag{12}$$

and

$$\begin{cases} z - z_0 = h^* \\ y = a_1x + b_1 \\ z = a_2x + b_2 \end{cases} \tag{13}$$

Thus, each radial-axial, cylindrical or horizontal hyperplane comprised between these two tracer locations defines a different system of equations, the solutions of which provide the coordinates of the intersections of the 3-D linear segment with the whole grid. If the number of such intersections is higher than 1, a dummy location is inserted in the middle between two consecutive intersections with the defined grid, i.e., inside each cell intersected by the fictitious segment of trajectory, as shown in Figure 6. Note that although the real grid used is based on cylindrical coordinates when, as in this example of Lagrangian data treatment, cylindrical vessels agitated by rotating impellers are being investigated, for purposes of clarity of the illustration, a grid composed of cubical cells is shown.

The entire sequence of Lagrangian data can be treated iteratively by considering every interval between two consecutive locations as an interruption, so that the particle tracer is characterized by transitions only between adjacent cells. The ratio of the total number of inserted dummy locations to the total number of original detected locations is a useful indication of the degree of fineness of the grid: a high number of dummy locations compared with the original number of detected locations would suggest that the grid is too fine. This operation improves the measurement accuracy of the time the tracer spends in each cell considerably, but the effect on the calculated velocity field is not expected to be significant unless the rate at which tracking is interrupted is particularly high or, equivalently, the grid is too fine.

Lagrangian velocity

A single Lagrangian data point consists of a temporal coordinate t and three spatial Cartesian coordinates x, y, and z, which are subsequently converted to the cylindrical coordinates ϑ, r, h with origin $\mathbf{O} = (x_0, y_0, z_0)$. Using this coordinate system with versors $\hat{\boldsymbol{\theta}}$, $\hat{\mathbf{r}}$, $\hat{\mathbf{h}}$, the Lagrangian velocity is:

$$\mathbf{v} = v_\vartheta\hat{\boldsymbol{\theta}} + v_r\hat{\mathbf{r}} + v_h\hat{\mathbf{h}} = r\frac{d\vartheta}{dt}\hat{\boldsymbol{\theta}} + \frac{dr}{dt}\hat{\mathbf{r}} + \frac{dh}{dt}\hat{\mathbf{h}} \cong r\alpha\hat{\boldsymbol{\theta}} + \beta\hat{\mathbf{r}} + \gamma\hat{\mathbf{h}} \tag{14}$$

where α, β, and γ are the numerically calculated time derivatives of the three cylindrical tracer coordinates which are contained in the arrays $[\vartheta_k]$, $[r_k]$, and $[h_k]$, respectively. The value of α, for instance, could be obtained using differences of ϑ and of t between two consecutive locations, i.e., the ratio between $\vartheta_{k+1} - \vartheta_k$ and $t_{k+1} - t_k$. Although almost negligible, a certain degree of spatial uncertainty characterizes each tracer location which may create small fictitious fluctuations in the velocity vector. By using the least squares method, a number of consecutive locations ($n_{\mathrm{LSM}} > 2$) could be used to minimize this effect. The values of α, β, and γ are then determined as the slopes of the best straight line representing the n_{LSM} points in the Cartesian planes $t\vartheta$, tr, and th, respectively. Thus, the Lagrangian velocity vector $\mathbf{v} = (v_\vartheta, v_r, v_h)$ is obtained numerically which is then associated with a new tracer position whose four time-space coordinates are

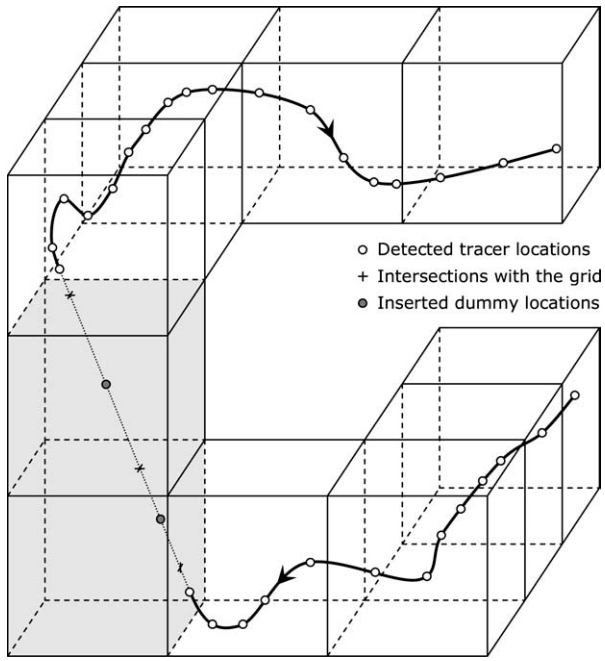

Figure 6. Illustration of the computational insertion of dummy locations: note that the real grid used is based on cylindrical coordinates, but cubical cells are shown here for clarity purposes.

recalculated by averaging the time coordinates of the n_{LSM} initial locations, and using the three straight lines having the newly calculated α, β, and γ as slopes to reobtain the three space coordinates. Where overlapping is allowed, the value of n_{LSM} does not significantly affect the length of the newly rewritten arrays $[t_k]$, $[\vartheta_k]$, $[r_k]$, and $[h_k]$ which are now associated with the arrays $[(v_\vartheta)_k]$, $[(v_r)_k]$, and $[(v_h)_k]$ containing the three cylindrical components of the Lagrangian velocity.

It should be noted that selecting the value of the parameter n_{LSM} is a matter of compromise, as n_{LSM} must be increased for an inaccurate tracer location and decreased for a fast tracer motion to avoid having an excessively smoothed trajectory and, hence, underestimated velocities. The sets of experimental data presented here were analyzed using $n_{LSM} = 3$–5.

Local Eulerian quantities

On the basis of the previously defined 3-D cylindrical grid with n_c equal volume cells, the instantaneous 3-D position assumed by the particle tracer (ϑ_k, r_k, h_k) can be converted into an integer index, i_k, designating the specific grid cell occupied by the tracer at time t_k. The spatial distribution of the number of detected tracer locations in a cell is then determined simply by counting the number of times each cell index appears in the new array $[i_k]$. If a sequence of equal indices i^* in $[i_k]$ is compacted into one single element equal to i^* (e.g., the sequence "7 7 7 7 7" is reduced to a single "7") a shorter array $[I_k]$ is created which, by means of the above counting process, leads to the distribution of the number of tracer visits. The two spatial distributions of the number of tracer visits, n_V, and detected locations, n_L, are conceptually different, therefore, the conversion of the Lagrangian velocity components into Eulerian velocities needs to be made taking into account such a distinction.

The time interval between the instants at which the particle tracer enters and leaves a cell may be different each time the tracer visits the same cell. Primarily for this reason, the number of detected locations is not constant at each visit during which a slow tracer is detected a higher number of times than a tracer moving at high speed. Consequently, a simple arithmetic mean of the Lagrangian velocities related to all the tracer locations within the same grid cell, i.e., the arithmetic mean of all the $(v_\vartheta)_k$, $(v_r)_k$, or $(v_h)_k$ corresponding to equal indices in $[i_k]$, would lead to an underestimated mean Eulerian velocity associated with the cell.

This estimation can be improved if, in a given cell, the mean Eulerian velocity is determined by first calculating the mean Lagrangian velocities, $\overline{v}_\vartheta$, $\overline{v}_r$, and $\overline{v}_h$, along the segment of trajectory intersecting with the cell at each visit, as shown in Figure 7, before averaging again by the number of visits. This procedure reduces the Lagrangian information to a single velocity vector associated with each tracer visit, regardless of the number of times the tracer is located and the duration of its sojourn in the cell. In computational terms, the arrays $[(v_\vartheta)_k]$, $[(v_r)_k]$, and $[(v_h)_k]$ are reduced to $[(\overline{v}_\vartheta)_k]$, $[(\overline{v}_r)_k]$, and $[(\overline{v}_h)_k]$ of the same length as $[I_k]$, by replacing each sequence which corresponds to equal indices in the parallel array $[i_k]$ with the arithmetic mean of the elements of the sequence itself. The mean Eulerian velocity components, u_ϑ, u_r, and u_h, are finally obtained in each cell by averaging all the velocity values in $[(\overline{v}_\vartheta)_k]$, $[(\overline{v}_r)_k]$, and $[(\overline{v}_h)_k]$ corresponding to the same cell index in $[I_k]$. It is worth noting that the same averaging process, performed using the square of such velocity values, leads to the standard deviations σ_ϑ, σ_r, and σ_h of the Eulerian velocity components in each cell.

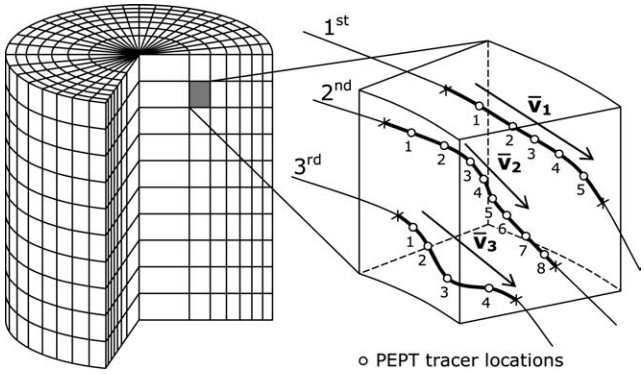

Figure 7. Illustration of the cylindrical grid used for the analysis of the Lagrangian data, and a grid cell with multiple tracer visits.

By using the previously obtained intersections of the tracer trajectory with the grid and their time coordinate, the time spent by the tracer in a cell during each visit, so-called residence time, is noted in a further array $[\delta t_k]$ having also the same length as $[I_k]$. Although intrinsically Lagrangian, this information can be transformed into an Eulerian distribution of the cumulative time, Δt, that the tracer spends within a given grid cell during an experiment, also called cumulative residence time or cumulative sojourn time. It is determined by adding together all the time values in $[\delta t_k]$ corresponding to the same cell index in the array $[I_k]$. Furthermore, maps of the mean residence time, $\overline{\delta t}$, can be obtained by dividing the time Δt by the number of tracer visits, n_V, in each cell.

Occupancy

The occupancy distribution of the tracer particle within the vessel offers an additional powerful tool for characterizing flow behavior within a mixing tank. Occupancy has traditionally been obtained by calculating the fraction of the total experimental time, t_∞, spent by the tracer in each cell during the experiment. Such a definition establishes a mathematical identity between occupancy and probability of presence of the particle tracer, but undesirably makes occupancy highly dependent on the density of the grid so that as the number of cells increases occupancy tends to zero. If the cells are chosen to have equal volume, however, this problem is circumvented by using the ergodic time defined as $t_E = t_\infty/n_c$, instead of the total experimental time t_∞. The ergodic time represents the time that the tracer would spend in any cell if the flow were single-phase and ergodic, an asymptotic status in which the flow tracer has equal probability of presence anywhere within the system. Thus, the local occupancy, O_E, can be defined as:

$$O_E = \frac{\Delta t}{t_E} \tag{15}$$

where Δt is the time that the tracer spends inside a given cell, i.e., the previously defined cumulative residence time. With

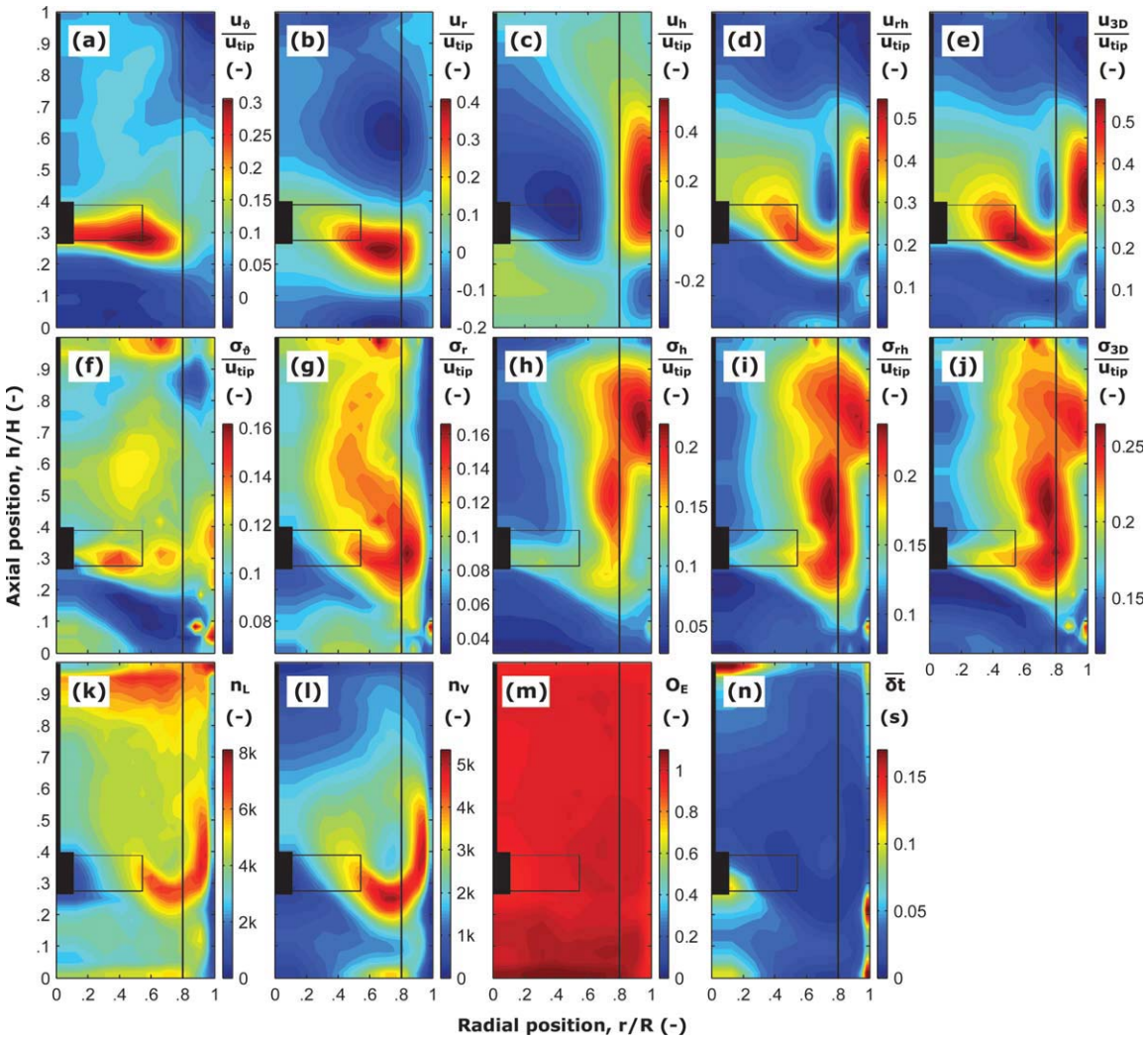

Figure 8. Azimuthally averaged radial-axial maps of various Eulerian quantities (see text for details) in a turbulent single-phase system: aqueous NaCl solution; *T* = 190 mm; PBTD; *D* = 105 mm (0.33 *T* off-bottom clearance); *N* = 220 rpm ($Re_{imp} \sim 40{,}000$).

[Color figure can be viewed in the online issue, which is available at wileyonlinelibrary.com.]

this definition, the average value of the vessel occupancy is 1 independently of the chosen number of grid-cells n_c. In addition, as shown below, Eq. 15 makes it possible to describe the spatial distribution of each phase component within a multiphase flow. Note that ergodicity is discussed in more detail in a further section below.

Eulerian maps

The 3-D cylindrical grid used is defined by three initial numerical parameters: the number of cells in the axial direction, n_h, in the radial direction, n_r, and in the azimuthal direction, n_ϑ. When n_ϑ is set to 1, each grid cell assumes the shape of a rectangular cross-section torus and, therefore, the related Eulerian datum is obtained using those Lagrangian data that can be ascribed to the torus regardless of their azimuthal coordinate ϑ. As a result, Eulerian data are intrinsically ensemble-averaged with respect to the azimuthal position and, although representing the whole mixing volume rather than a single 2-D vertical section, such data can be presented in the form of 2-D radial-axial maps. Examples of such maps are depicted in Figure 8 which presents a set of quantities obtained within a turbulent single-phase system (aqueous NaCl solution) from one long single particle tracking experiment lasting $\sim$45 min. While distributions of the three velocity components (u_ϑ, u_r, u_h) normalized by the tip speed of the turbine, $u_{tip} = n$ND, are illustrated in Figures 8a–c, the normalized magnitudes of the radial-axial 2-D velocity vector $\mathbf{u_{rh}}$ and the total 3-D velocity vector $\mathbf{u_{3D}}$ are mapped in Figures 8d and 8e, respectively. In the case of a solid–liquid system, these velocity maps can be generated for each phase. Furthermore, local time-averaged particle slip velocities can be estimated by locally subtracting the velocity of the solid phase from that of the liquid. This information is of real value to processing applications involving the transfer of heat or mass, such as in chemical reactions or the sterilization of particulate food mixtures. A crude assumption, often used in practice takes the free terminal

settling velocity of the particle as a representative of its mean slip velocity.[26,27] Although the values yielded by the described methodology are likely to be much more realistic, it is currently difficult to be certain about the accuracy of these estimations given that information on particle rotation and turbulent velocity fluctuations (including whether in or out of phase) of the two phases is still missing.

Furthermore, as pointed out above, the standard deviations σ_ϑ, σ_r, and σ_h of the Eulerian velocity components are also determined in each cell and their normalized values together with those of σ_{rh} and σ_{3D} are plotted in Figures 8f–j these quantities provide information on the local velocity fluctuations. It should be noted that one of the limitations of this approach is the frequency response which is directly related to the Lagrangian concepts of circulation and residence times, further discussed below in the Lagrangian statistical analysis section. Because such a frequency is intrinsically relatively low, the values of standard deviation obtained by PEPT do not currently provide a realistic measure of turbulence as those yielded by Eulerian laser-based techniques do.

Using the arrays $[i_k]$ and $[I_k]$, the number of tracer locations n_L and tracer visits n_V are obtained in each cell providing the widely different maps in Figures 8k and 8l which confirm, as discussed above, that considering the number of tracer locations instead of visits may lead to a significant underestimation of the mean Eulerian velocities. The Lagrangian measurements enable Δt to be computed leading to plots of occupancy, O_E, and average residence time, $\overline{\delta t}$, as shown in Figures 8m and 8n, respectively. As expected, in a single-phase flow the occupancy distribution is almost uniform and consequently the average residence time is practically proportional to the inverse of the number of visits.

Phase distribution in multiphase flow

Considering for example a monodisperse solid–liquid system, the infinitesimal probability, $p(\mathbf{P})dV$, that a specific small solid particle is inside an infinitesimal volume element dV is a function of the particle position $\mathbf{P} = (x, y, z)$ and can be expressed from two different points of view. From the Lagrangian point of view, it is the ratio of the infinitesimal time dt that the tracer spends inside dV, to the total time of detection t_∞; in Eulerian terms, however, it is the ratio of the number of solid particles dn, contained in dV, to the total number of such particles in the vessel n. Consequently, it follows that:

$$\left\{ p(\mathbf{P})dV = \frac{dt}{t_\infty} \text{ and } p(\mathbf{P})dV = \frac{dn}{n} \right\} \Rightarrow \frac{dt}{t_\infty} = \frac{dn}{n} \quad (16)$$

Introducing the volume of a single particle V_P, the infinitesimal solid volume dV_S in dV, the total solid volume present in the tank V_S, the local time-averaged solid volume concentration c, the mean solid volume concentration in the vessel C, and the total volume of the multiphase suspension V_T, yields:

$$\frac{dn}{n} = \frac{V_P dn}{V_P n} = \frac{dV_S}{V_S} = \frac{cdV}{CV_T} \quad (17)$$

Combining Eqs. 16 and 17 leads to a clear correlation between the time that the tracer spends inside dV and the local time-averaged solid volume concentration, that is:

$$\frac{dt}{t_\infty} = \frac{cdV}{CV_T} \quad (18)$$

If the cell volume, ΔV, in the grid is uniform, the total number of grid cells is then $n_c = V_T/\Delta V$, and rewriting the above equation in discrete terms gives:

$$\frac{\Delta t}{t_\infty} = \frac{c\Delta V}{CV_T} \Rightarrow \frac{\Delta t}{t_E} = \frac{c}{C} \quad (19)$$

Defining, according to Eq. 15, the occupancy O_E as the ratio of time that the tracer spends inside a cell to the ergodic time, Eq. 19 then becomes:

$$O_E = \frac{c}{C} \quad (20)$$

Note that while this relationship has been derived for the discrete phase in a monodisperse system, it is equally valid for the fluid component as well as for each component in a suspension containing multiple liquid or solid traceable components. The immediate important consequence of Eq. 20 is that, in addition to phase velocity, it is now possible to fully map by Lagrangian tracking the local time-averaged concentration of each flow component in a multiphase system. For example, the time-averaged volume concentration of each of the two solid components and of the liquid in binary solid–liquid suspensions has recently been mapped experimentally using single particle tracking and newly developed three-component concentration maps.[23]

As shown in Figure 8m, the occupancy map in a turbulent single-phase system is almost uniform and $O_E \sim 1$, which is in agreement with Eq. 20 because in a single-phase system the time-averaged phase concentration is 100% everywhere. In a turbulent single-phase system, the approximation $O_E = 1$ becomes gradually more accurate as the experimental runtime t_∞ is lengthened, strictly tending to infinity (here t_∞ was mostly 30–45 min). Consequently, the uniformity of the occupancy map in a turbulent single-phase system could be used as an index to determine if a long enough runtime t_∞ has been selected.

Lagrangian Statistical Analysis

Lagrangian tracking of the long-term trajectory of a fluid follower provides data which can be exploited to visualize flow structures and obtain statistical information on the mixing performance. The popular concept of residence time distribution (RTD) in a continuous flow system was extended by Villermaux[10] who introduced the concept of TLD based on the distance covered by fluid elements or tracer particles carried by the flow from the inlet to the outlet. By using Lagrangian data, it is also possible to apply these concepts to a batch system such as a stirred vessel.

The concept of residence time in a continuous system can be extended to a batch system by considering the time interval related to the multiple trajectories followed by a Lagrangian tracer from the point at which it leaves a given reference plane or volume to the point where it returns back to it. If the selected plane is a horizontal plane close to the impeller discharge, the concept of residence time is replaced by

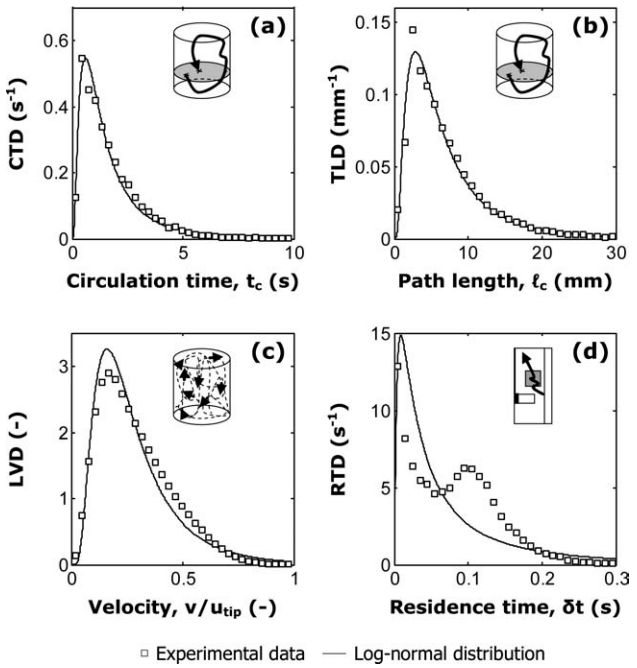

Figure 9. Probability density distributions in a single-phase system: aqueous NaCl solution; T = 190 mm; PBTD; D = 105 mm (0.33 T off-bottom clearance); N = 220 rpm ($Re_{imp} \sim$ 40,000); (a) circulation time distribution for the horizontal plane at 0.25 H; (b) circulation trajectory length distribution for the horizontal plane at 0.25 H; (c) Lagrangian velocity magnitude distribution; (d) residence time distribution within the shaded area.

the circulation time t_c which can be computed by solving systems of equations analogous to the system in Eq. 13 with an additional equation including the temporal coordinate. The values of t_c obtained tend to distribute according to the statistical log-normal distribution as shown in Figure 9a for a turbulent single-phase system. Such a probability density distribution is called circulation time distribution (CTD).

The trajectory length during each recirculation can also be measured obtaining the path length ℓ_c whose distribution, the TLD, is illustrated in Figure 9b. Similar to the CTD, the TLD is also very well represented by a log-normal distribution. Additional statistical distributions can be obtained by analyzing the Lagrangian velocity components, exploiting the arrays $[(v_\vartheta)_k]$, $[(v_r)_k]$, and $[(v_h)_k]$, or by using the Lagrangian velocity magnitude. The Lagrangian velocity distribution, i.e., the distribution of the 3-D Lagrangian velocity magnitude v, is presented in Figure 9c which again shows a very good agreement with the log-normal distribution.

The spatial distribution of the mean residence time $\overline{\delta t}$ within a grid cell, illustrated above in Figure 8n, is obtained by averaging in each cell the values sequentially stored in the array $[\delta t_k]$. Alternatively, this quantity can be locally studied by considering the statistical distribution of the residence time δt related to a selected grid cell or, more generally, to any geometrically defined volume. The RTD shown in Figure 9d was obtained for a squared cross-section torus ($0.3\ R < r < 0.5\ R$ and $0.5\ H < h < 0.7\ H$) by recording the time, δt, that the particle tracer spends within this toroidal volume during each visit. Contrary to the other distributions, the RTD for the examined volume is not well represented by a log-normal distribution; this effect is probably due to the fact that the closed surface bounding the volume is imaginary and the tracer can penetrate such surface at any point generating, therefore, a high number of short residence times δt which are close to zero.

Other examples of quantities and maps that can be obtained by virtue of Lagrangian particle tracking are local and global entropy mixing indices[22] by using the Shannon entropy concept, the decorrelation time[8,22] by autocorrelating the particle tracer trajectory, and Poincaré maps[28] via a computational process based on the mathematical concept of Poincaré section and the solution of numerous systems of equations similar to the systems in Eqs. 11–13.

Methods of Validating Measurements

Ergodicity

The theoretical premise which guarantees that a tracer is representative of all the solid or liquid phase is referred to as ergodicity or iso-probability condition. As already mentioned above, for a single-phase system, such a condition implies an equal probability of tracer presence at every point in the flow. In a multiphase system, however, the total probability for all phases is required to be uniform, i.e., the sum of probabilities of presence (weighted by the inverse of the time-averaged phase volume concentration) of all components of the system must be the same everywhere. Ergodicity is a theoretical state which can be approached only after an infinite tracking time. However, it can be mathematically shown that, if the probability of tracer visit is sufficiently high everywhere, ergodicity can be assumed when the trajectory of the tracer is recorded over a sufficiently long time during which adequate data resolution is achieved in every region.[8] The Lagrangian tracking time used was $\geq$30 min in all the experiments, which was long enough to acquire a sufficient amount of data in all regions of the vessel. Hence, ergodicity could be safely assumed given that in such systems the probability of visit is sufficiently uniform by virtue of the open geometry of the vessel where all regions are more or less equally accessible to the tracer. However, to assess the accuracy of the ergodic assumption, the probability of tracer presence can be calculated and its uniformity verified. On the basis of Eq. 15, when the cells have equal volume the occupancy is proportional to the probability of tracer presence $\Delta t/t_\infty$ and, consequently, Figure 8m for example shows that the tracer has practically an equal probability of presence everywhere within the vessel for a single-phase system.

Mass continuity in a multiphase system

Mass continuity is an important tool for checking the accuracy and reliability of flow data including Lagrangian measurements. The net mass flux through a volume bounded by a closed surface S should be zero, thus

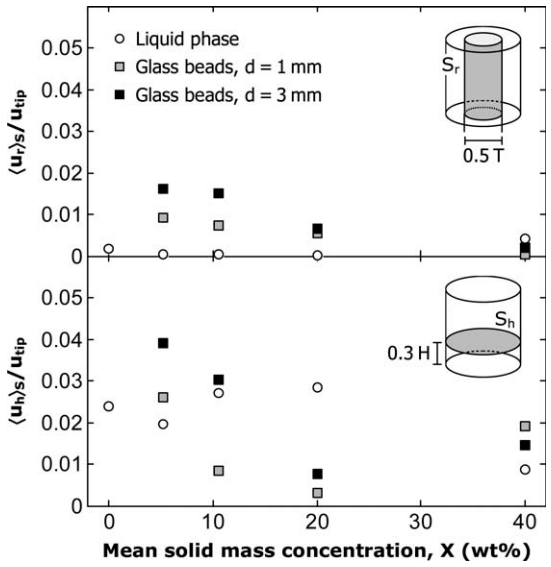

Figure 10. Mass continuity verification for PEPT in a binary suspension of glass beads in aqueous NaCl solution: normalized radial and axial velocities averaged over surfaces S_r (of diameter 0.5 T) and S_h (0.3 H off the base), respectively; T = 288 mm; PBTD; D = 144 mm (0.25 T off-bottom clearance); $N = N_{js}$; Re_{imp} > 100,000.

$$\sum_S \mathbf{u_{3D}} \cdot \Delta \mathbf{S} \cong 0 \tag{21}$$

Calculations can be made by considering a closed cylindrical surface S with the same vertical axis, base and diameter as the tank but of a shorter height. Because of $\mathbf{u_{3D}}$ being zero over the external surface of the vessel or being parallel to it, the term $\mathbf{u_{3D}} \cdot \Delta \mathbf{S}$ is zero everywhere except in the horizontal plane across the tank, so that S can be reduced to such a plane, S_h, and Eq. 21 is reduced to a zero average of axial velocities across the horizontal plane considered. A similar situation can be envisaged where S is a closed cylindrical envelope with the same vertical axis and height as the tank but with a smaller diameter; Eq. 21 then becomes a zero average of radial velocities across the lateral surface, S_r, of the considered cylindrical volume. Testing, for instance, the set of Lagrangian data collected in binary suspensions of up to 40 wt % glass particles, a very good verification of the mass continuity was obtained as calculations gave a velocity average close to zero, generally less than $0.03 u_{tip}$, as demonstrated in Figure 10. For perfect mass continuity, the first term in Eq. 21 and, thus, the velocity values reported in Figure 10 should be identically equal to zero.

Two-dimensional comparison of Lagrangian-Eulerian and Eulerian data

Comparison between time-averaged Eulerian velocity maps obtained via Lagrangian tracking and a well-established optical technique such as PIV is a time consuming but highly reliable way to validate the Lagrangian data collected, their analysis, and the technique of measurement used itself. Unfortunately, the optical nature of the PIV technique tends to restrict comparison to transparent single-phase systems. Even very dilute solid concentrations ($\sim$1 wt %) tend to make the suspension partially opaque even with refractive index matching, compromising thus the reliability and applicability of the PIV technique.

To apply this comparison tool, two time-averaged and azimuthally averaged Eulerian velocity vector plots obtained by PIV and PEPT in a single-phase aqueous NaCl solution are compared in Figure 11 showing a very good agreement. Both of the two radial-axial maps are representative of the whole mixing vessel since n_9 was set to 1 in the analysis of the PEPT data, and the PIV data were collected in planes at 5° intervals over a 90° sector between two adjacent baffles and azimuthally averaged. A more detailed quantitative comparison is shown in Figure 12 where multiple radial and vertical profiles of the radial and axial velocity components u_r and u_h are compared and the agreement appears to be excellent throughout.

Conclusions

The purpose of this work was to present a detailed methodology developed for the analysis and validation of Lagrangian data obtained from single particle tracer trajectories, particularly when undertaking mixing studies in cylindrical stirred vessels. Such a methodology has been successfully applied to the analysis of data collected in various single-phase and multiphase systems using PEPT. Thus, it has been shown that the data can be used to resolve the Lagrangian trajectory under turbulent flow conditions and the 3-D flow

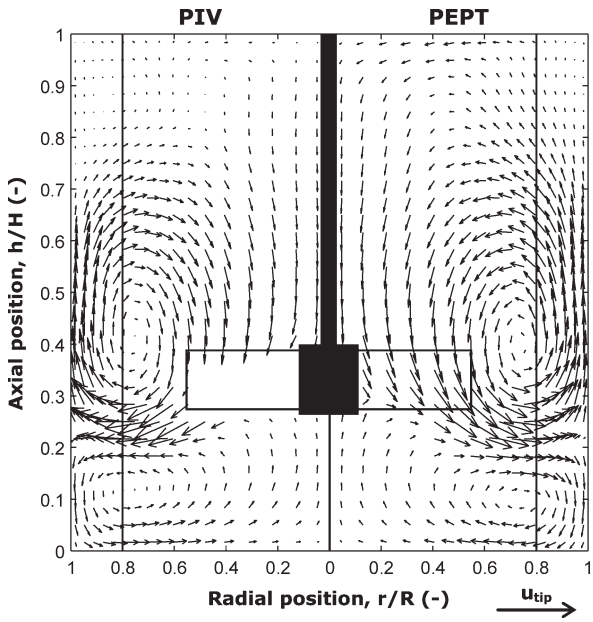

Figure 11. Comparison of time-averaged and azimuthally averaged radial-axial velocity vector plots obtained by PIV and PEPT in a single-phase system: aqueous NaCl solution; T = 190 mm; PBTD; D = 105 mm (0.33 T off-bottom clearance); N = 220 rpm ($Re_{imp} \sim$ 40,000).

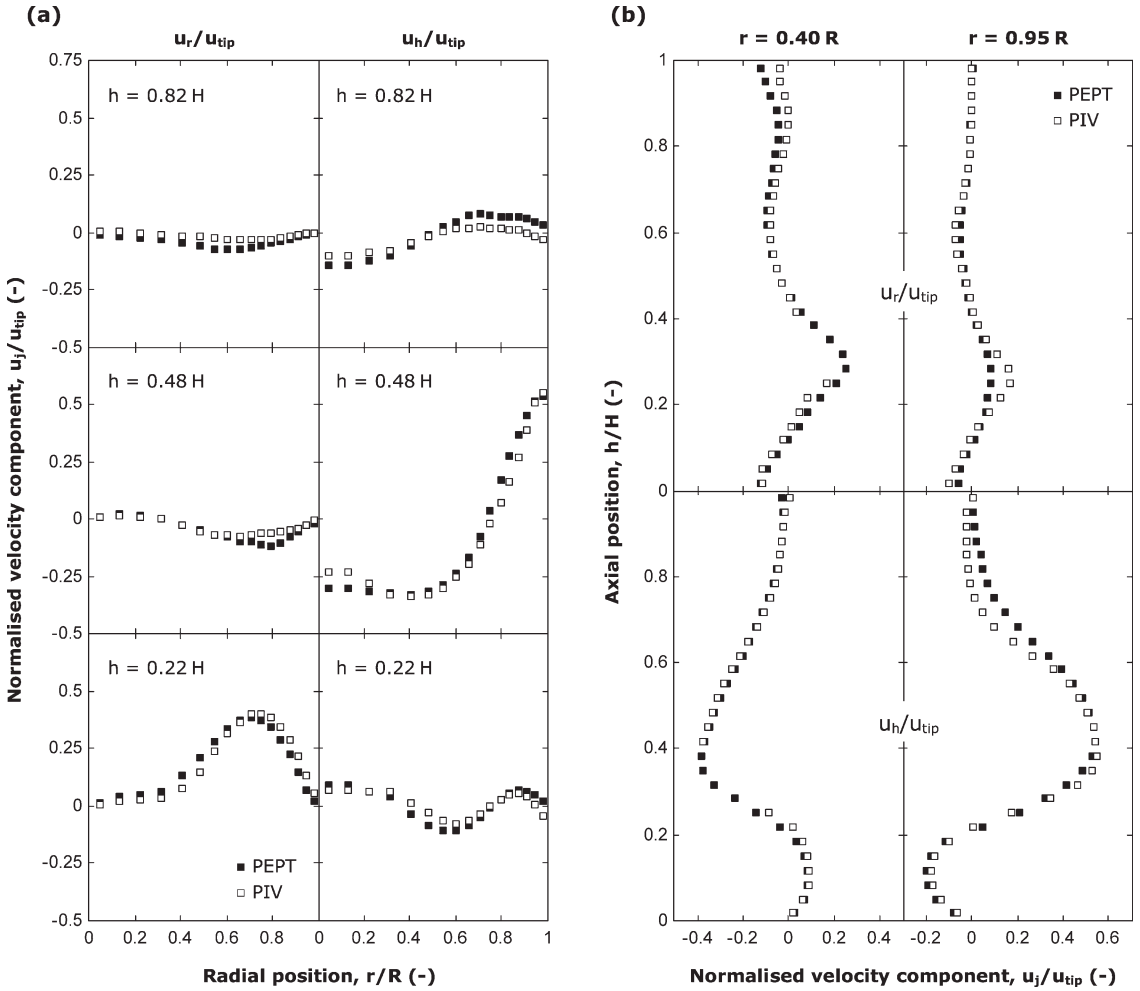

Figure 12. Time-averaged and azimuthally averaged velocity profiles obtained by PIV and PEPT in a single-phase system: aqueous NaCl solution; T = 190 mm; PBTD; D = 105 mm (0.33 T off-bottom clearance); N = 220 rpm ($Re_{imp} \sim$ 40,000).

structure within the cavern formed around the agitator when mixing a viscoplastic fluid. It has also been shown how to analyze Lagrangian multiphase data to give detailed Eulerian descriptions of various mixing parameters for the liquid phase and each solid size including the full 3-D velocity field, local occupancy and residence time distributions as well as their time-averaged spatial distribution. Techniques for obtaining other features have also been outlined to give further insight such as the computation of Lagrangian frequency distributions and the use of hyperplanes to estimate circulation times and trajectory lengths. One of the important tools developed here enables the mass continuity of each tracked component within a multiphase mixture to be accurately tested, which is crucial for establishing the reliability and accuracy of the measurements. An additional simple but decisive reliability test for stirred vessels compares the Eulerian flow data deduced by Lagrangian particle tracking with analogous data obtained by a well-established Eulerian optical technique. In particular, Eulerian time-averaged and azimuthally averaged velocity fields and profiles have been obtained in a transparent liquid by PIV and compared with the same Eulerian information after the Lagrangian tracking by PEPT had been converted to Eulerian flow data by applying the methodology outlined here. Excellent agreement between the two techniques was obtained. It is expected that the methods of data analysis developed in this work could be applied to a wide range of single-phase or multiphase mixing phenomena in stirred vessels using Lagrangian measuring techniques, and also to computational studies of similar problems when for example using CFD to simulate Lagrangian particle tracking.

Acknowledgments

This research was funded by The Engineering and Physical Sciences Research Council (UK) through Grant GR/S70517/01. We thank Prof. D.J. Parker and Dr. X. Fan of the Positron Imaging Centre at The University of Birmingham for their assistance with the PEPT experiments.

Notation

a_1, a_2 = slope coefficients of 3-D straight line
b_1, b_2 = intercept coefficients of 3-D straight line (m)
c = time-averaged local volume concentration of solids

C = mean volume concentration of solids
d = particle diameter (m)
D = impeller diameter (m)
E_G = geometric efficiency
H = height of the suspension (m)
i, I = cell indices
j = generic cylindrical direction
k = location counter
ℓ_c = circulation trajectory length (m)
L_D, H_D, S_D = dimensions of detection volume (m)
n = number of particles in the vessel
n_c = number of grid cells
n_ϑ, n_r, n_h = number of cells in the cylindrical directions
n_L = number of locations per cell
n_{LSM} = number of consecutive locations
n_s = number of particle size fractions
n_V = number of visits per cell
N = impeller rotational speed (s^{-1})
N_{js} = minimum speed for particle suspension (s^{-1})
$\mathbf{O}$ = origin of cylindrical coordinates vector (|m|)
O_E = occupancy
p = probability density function (m^{-3})
$\mathbf{P}$ = tracer location vector (|m|)
q = index of summation in Eq. 10
q_b = fraction of black pixels
r, h = radial-axial cylindrical coordinates (m)
r_c = centering circumference radius (m)
R = vessel radius (m)
Re_{imp} = impeller Reynolds number ($N_{js}D^2/\nu$)
S = surface area (m^2)
t = time (s)
t_∞ = PEPT runtime (s)
t_c = circulation time (s)
t_E = ergodic time (s)
T = vessel diameter (m)
u_ϑ, u_r, u_h = time-averaged cylindrical Eulerian velocities (m s^{-1})
$\mathbf{u_{3D}}$ = time-averaged Eulerian velocity vector (|m s^{-1}|)
$\mathbf{u_{rh}}$ = time-averaged radial-axial Eulerian velocity vector (|m s^{-1}|)
u_{tip} = impeller tip speed (m s^{-1})
$\mathbf{v}$ = tracer Lagrangian velocity vector (|m s^{-1}|)
v = magnitude of tracer Lagrangian velocity (m s^{-1})
v_ϑ, v_r, v_h = tracer Lagrangian velocity components (m s^{-1})
$\overline{v}_\vartheta, \overline{v}_r, \overline{v}_h$ = mean velocity components in a visit (m s^{-1})
V = volume (m^3)
V_P = particle volume (m^3)
V_S = volume of solids in the vessel (m^3)
V_T = total suspension volume (m^3)
x, y, z = Cartesian coordinates (m)
x_0, y_0, z_0 = centre of vessel base (m)
X = mean mass concentration of solids

Greek letters

α = numerical time derivative of ϑ (rad s^{-1})
β, γ = numerical time derivatives of r and h (m s^{-1})
δt = residence time (s)
$\overline{\delta t}$ = mean residence time (s)
ϑ = azimuthal coordinate (rad)
θ, ϕ = angular coordinates of spherical system (rad)
$\hat{\boldsymbol{\vartheta}}, \hat{\mathbf{r}}, \hat{\mathbf{h}}$ = versors of cylindrical coordinate system
ν = kinematic liquid viscosity (m^2 s^{-1})
ρ = radial spherical coordinate (m)
$\sigma_\vartheta, \sigma_r, \sigma_h$ = standard deviation of Eulerian velocities (m s^{-1})
σ_{3D} = standard deviation of $|\mathbf{u_{3D}}|$ (m s^{-1})
σ_{rh} = standard deviation of $|\mathbf{u_{rh}}|$ (m s^{-1})
Ω = solid angle (sr)

Abbreviations

CTD = circulation time distribution
LVD = Lagrangian velocity distribution
PBT = pitched blade turbine
PBTD = down-pumping PBT
PBTU = up-pumping PBT
PEPT = positron emission particle tracking
PIV = particle image velocimetry
PSD = particle-size distribution
RTD = residence time distribution
TLD = trajectory length distribution

Literature Cited

1. Ducci A, Yianneskis M. Turbulence kinetic energy transport processes in the impeller stream of stirred vessels. *Chem Eng Sci*. 2006;61:2780–2790.
2. Chung KHK, Barigou M, Simmons MJH. Reconstruction of 3-D flow field inside miniature stirred vessels using a 2-D PIV technique. *Chem Eng Res Des*. 2007;85:560–567.
3. Chung KHK, Simmons MJH, Barigou M. Angle-resolved particle image velocimetry measurements of flow and turbulence fields in small-scale stirred vessels of different mixer configurations. *Ind Eng Chem Res*. 2009;48:1008–1018.
4. Morud KE, Hjertager BH. LDA measurements and CFD modelling of gas-liquid flow in a stirred vessel. *Chem Eng Sci*. 1996;51:233–249.
5. Unadkat H, Rielly CD, Hargrave GK, Nagy ZK. Application of fluorescent PIV and digital image analysis to measure turbulence properties of solid–liquid stirred suspensions. *Chem Eng Res Des*. 2009;87:573–586.
6. LaRoche RD. *Evolution of CFD as a tool for chemical engineering*. In: *Proceedings of CFD in Chemical Reaction Engineering IV*, Barga, Italy, June 19–24, 2005.
7. Lavezzo V, Verzicco R, Soldati A. Ekman pumping and intermittent particle resuspension in a stirred tank reactor. *Chem Eng Res Des*. 2009;87:557–564.
8. Wittmer S, Falk L, Pitiot P, Vivier H. Characterization of stirred vessel hydrodynamics by three dimensional trajectography. *Can J Chem Eng*. 1998;76:600–610.
9. Rammohan AR, Kemoun A, Al-Dahhan MH, Dudukovic MP. A Lagrangian description of flows in stirred tanks via computer automated radioactive particle tracking. *Chem Eng Sci*. 2001;56:2629–2639.
10. Villermaux J. Trajectory length distribution (TLD), a novel concept to characterize mixing in flow systems. *Chem Eng Sci*. 1996;51:1939–1946.
11. Doucet J, Bertrand F, Chaouki J. A measure of mixing from Lagrangian tracking and its application to granular and fluid flow systems. *Chem Eng Res Des*. 2008;86:1313–1321.
12. Barigou M. Particle tracking in opaque mixing systems: an overview of the capabilities of PET and PEPT. *Chem Eng Res Des*. 2004; 82:1258–1267.
13. Parker DJ, Leadbeater TW, Fan X, Hausard MN, Ingram A, Yang Z. Positron imaging techniques for process engineering: recent developments at Birmingham. *Meas Sci Technol*. 2008;19:094004 (10pp).
14. Fangary YS, Barigou M, Seville JPK, Parker DJ. Fluid trajectories in a stirred vessel of non-Newtonian liquid using positron emission particle tracking. *Chem Eng Sci*. 2000;55:5969–5979.
15. Fangary YS, Barigou M, Seville JPK, Parker DJ. A Langrangian study of solids suspension in a stirred vessel by positron emission particle tracking (PEPT). *Chem Eng Technol*. 2002;25:521–528.
16. Guida A, Fan X, Parker DJ, Nienow AW, Barigou M. Positron emission particle tracking in a mechanically agitated solid-liquid suspension of coarse particles. *Chem Eng Res Des*. 2009;87:421–429.
17. Guida A, Nienow AW, Barigou M. PEPT measurements of solid-liquid flow field and spatial phase distribution in concentrated monodisperse stirred suspensions. *Chem Eng Sci*. 2010;65:1905–1914.
18. Fan X, Parker DJ, Smith MD. Enhancing F-18 uptake in a single particle for positron emission particle tracking through modification of solid surface chemistry. *Nucl Instrum Methods Phys Res A*. 2006;558:542–546.
19. Fan X, Parker DJ, Smith MD. Labelling a single particle for positron emission particle tracking using direct activation and ion-exchange techniques. *Nucl Instrum Methods Phys Res A*. 2006;562: 345–350.
20. Parker DJ, Forster RN, Fowles P, Takhar PS. Positron emission particle tracking using the new Birmingham positron camera. *Nucl Instrum Methods Phys Res A*. 2002;477:540–545.

21. Parker DJ, Broadbent CJ, Fowles P, Hawkesworth MR, Mcneil P. Positron emission particle tracking—a technique for studying flow within engineering equipment. *Nucl Instrum Methods Phys Res A*. 1993;326:592–607.
22. Guida A, Nienow AW, Barigou M. Shannon entropy for local and global description of mixing by Lagrangian particle tracking. *Chem Eng Sci*. 2010;65:2865–2883.
23. Guida A, Nienow AW, Barigou M. Mixing of dense binary suspensions: multi-component hydrodynamics and spatial phase distribution by PEPT. *AIChE J*. DOI 10.1002/aic.12456.
24. Zwietering TN. Suspending of solid particles in liquid by agitators. *Chem Eng Sci*. 1958;8:244–253.
25. Adams LW, Barigou M. CFD analysis of caverns and pseudo-caverns developed during mixing of non-Newtonian fluids. *Chem Eng Res Des*. 2007;85:598–604.
26. Nienow AW. *The mixer as a reactor–liquid/solid systems*. In: Harnby N, Edwards MF, Nienow AW, editors. *Mixing in the Process Industries*, 2nd ed. London: Butterworth-Heinemann, 1997: 394–411.
27. Atiemo-Obeng VA, Penney WR, Armenante P. *Solid-liquid mixing*. In: Paul EL, Atiemo-Obeng VA, Kresta SM, editors. *Handbook of Industrial Mixing*. New Jersey: Wiley, 2004:543–584.
28. Barigou M, Chiti F, Pianko-Oprych P, Guida A, Adams L, Fan X, Parker DJ, Nienow AW. Using positron emission particle tracking (PEPT) to study mixing in stirred vessels: validation and tackling unsolved problems in opaque systems. *J Chem Eng Jpn*. 2009; 42:839–846.

Manuscript received Oct. 7, 2010, and revision received Jan. 10, 2011.